JACS
JOURNAL OF THE AMERICAN CHEMICAL SOCIETY

In Situ Hybridization of Superparamagnetic Iron-Biomolecule Nanoparticles

Nafiseh Moghimi,[†] Apraku David Donkor,[†] Mamata Mohapatra,[†,‡] Joseph Palathinkal Thomas,[†] Zhengding Su,[§] Xiaowu (Shirley) Tang,[†] and Kam Tong Leung*[,†]

[†]Department of Chemistry, University of Waterloo, Waterloo, Ontario, Canada N2L3G1

[‡]Department of Hydro and Electro Metallurgy, Institute of Minerals and Materials Technology, Council of Scientific and Industrial Research, Bhubaneswar 751 013, Odisha, India

[§]Danny Thomas Research Center, St Jude Children's Research Hospital, Memphis, Tennessee 38103, United States

Supporting Information

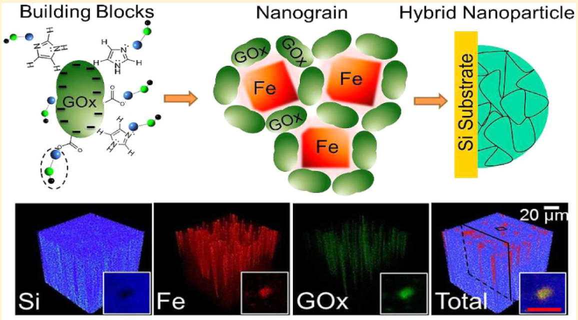

ABSTRACT: The increase in interest in the integration of organic–inorganic nanostructures in recent years has promoted the use of hybrid nanoparticles (HNPs) in medicine, energy conversion, and other applications. Conventional hybridization methods are, however, often long, complicated, and multistepped, and they involve biomolecules and discrete nanostructures as separate entities, all of which hinder the practical use of the resulting HNPs. Here, we present a novel, in situ approach to synthesizing size-specific HNPs using Fe-biomolecule complexes as the building blocks. We choose an anticancer peptide (p53p, MW 1.8 kDa) and an enzyme (GOx, MW 160 kDa) as model molecules to demonstrate the versatility of the method toward different types of molecules over a large size range. We show that electrostatic interaction for complex formation of metal hydroxide ion with the partially charged side of biomolecule in the solution is the key to hybridization of metal-biomolecule materials. Electrochemical deposition is then used to produce hybrid NPs from these complexes. These HNPs with controllable sizes ranging from 30 nm to 3.5 μm are found to exhibit superparamagnetic behavior, which is a big challenge for particles in this size regime. As an example of greatly improved properties and functionality of the new hybrid material, *in vitro* toxicity assessment of Fe-GOx HNPs shows no adverse effect, and the Fe-p53p HNPs are found to selectively bind to cancer cells. The superparamagnetic nature of these HNPs (superparamagnetic even above the size regime of 15–20 nm!), their biocompatibility, and the direct integration approach are fundamentally important to biomineralization and general synthesis strategy for bioinspired functional materials.

INTRODUCTION

Composite systems of biomolecules and metal nanostructures combine the evolution-optimized molecular recognition capability of biomolecules with the novel optical, electronic, and catalytic properties of nanomaterials. These composite systems offer excellent prospect for developing a new generation of multifunctional bioelectronic devices. In the past decade, there has been substantial progress in the use of biomolecule-nanostructure composites in electrochemical biosensors, electronic nanocircuitry, and even nanodevices.[1−4] In conventional approaches, the biomolecules and metal nanostructures are treated as separate entities. Biointegration into nanostructures could only be obtained by immobilization of biomolecules on the inner and/or outer surfaces of the nanostructures, including polymer matrices, inorganic supports, and nanoparticles (NPs).[5−7] Well-established techniques based on physical adsorption, electrostatic binding, specific recognition, and covalent coupling have often been used for immobilization.[8−11] In particular, adsorption of proteins on NPs has been achieved through electrostatic interactions between the partially charged amino acid side groups of the protein and the appropriate component with opposite polarity on the NPs. The latter component could be a functional group of a linker molecule precoated on the NPs or a partially charged site on the nanostructure.[12,13] There is a general lack of study on biointegration into the nanostructure during growth. Such studies can provide fundamental information about the nature of this integration (including bonding, interactions, and growth mechanism), which could lead to a new class of bionanomaterials. With many applications in biosensor research, food industry, and renewable fuel cells,[14−18] glucose oxidase (GOx, with MW of 160 kDa) is a popular model biomolecule for studying self-organization of nanostructures on biomolecules and of biomolecules on other surfaces. In the limited number of studies on conjugating GOx onto NPs by electrostatic interaction,[19,20] the NPs were synthesized first and GOx were subsequently allowed to interact with the NPs. Even in the

Received: May 25, 2014
Published: July 3, 2014

earlier work on the co-electrodeposition of GOx and gold NPs,[21,22] separate GOx and pregrown NPs were used. To date, direct incorporation of biomolecules into the nanostructures during growth remains challenging, because the presence of an aqueous medium with a mild pH (as required by the biomolecules) and the need for low growth temperature (preferably below room temperature) are not conducive to nanostructure growth. Although the chelation and complexation of metal ions with GOx have been widely studied, there is no report on using metal ions-GOx complexes directly to synthesize hybrid nanoparticles (HNPs).

The same hybridization approach can also be easily extended to incorporate other biomolecules, even with dramatically different sizes, in these HNPs. The anticancer p53 peptide (p53p, with MW of 1.8 kDa) is a promising drug for most cancers because it can bind to both Mdm2 and MdmX in cancer cells.[23] Almost 50% of cancers are caused by overexpressed Mdm2 and MdmX as they inhibit the tumor suppressor, p53p.[24,25] Attaching p53p to magnetic NPs that can be delivered to targeted tumor sites is a breakthrough in anticancer therapeutics.

In this work, we report the successful synthesis of Fe-GOx and Fe-p53p HNPs by using Fe-GOx and Fe-p53p complexes directly as the building blocks, without involving pregrown Fe NPs followed by biomolecule coating. We further demonstrate that these HNPs consist of Fe nanocrystallites binding together by biomolecules similar to a stone-and-mortar architecture. We make these Fe-biomolecule complexes by adjusting the pH of the aqueous solution to above the isoelectric point of GOx or p53p, in which the negatively charged amino acids on the surface of the biomolecule electrostatically interact with the positive Fe ions. By conducting the co-electrodeposition at 4 °C, we produce Fe-GOx and Fe-p53p HNPs that show superparamagnetic properties even when these HNPs are as large as a few hundred nanometers, while preserving the bioactivities of GOx and p53p at the same time. The Fe-GOx HNPs also exhibit remarkable biocompatibility to human hepatoma cells (liver cells). This method of producing size-specific superparamagnetic HNPs has the important advantage of attaining the desired size while eliminating the postfunctionalization (coating) step to achieve the size needed for practical use of these superparamagnetic NPs. We show that in the present hybridization method GOx not only maintains its enzymatic activities but also acts as a protective shell from oxidation for metallic Fe nanocrystallites. As a further practical demonstration, we also show that p53p remains active after hybridization and can bind to Mdm2, which confirms the generality of the present approach. Isolation of Fe nanocrystallites by GOx or p53p introduces extraordinary magnetic property for large HNPs (i.e., superparamagnetism in large sizes). Electrochemical hybridization of metals with biomolecules therefore offers a novel approach to developing cell-friendly magnetic HNPs with homogeneously distributed magnetic nanocrystallites and biomolecules inside. The present method is however not limited to electrochemical reduction, and Fe-biomolecule complex reduction with any other reducing agent would also be possible. These HNPs promise potential applications not only as magnetic contrast agents but also in targeted slow-release drug delivery systems.

■ MATERIALS AND METHODS

Preparation of the HNPs. Fe-GOx HNPs were prepared by co-electrodeposition of Fe and GOx on a H-terminated Si(100) substrate in a three-electrode cell using an electrochemical workstation (CH Instruments 660A). A silicon chip (15 × 2.5 mm^2, 0.4 mm thick), precut from a Si(100) wafer (p-type, B-doped, with a resistivity of 0.01−0.02 Ω·cm), was used as the working electrode after it was cleaned using the RCA method. It was then H-terminated by dipping in a 2% aqueous HF solution. A standard Ag/AgCl electrode was used as the reference electrode and a Pt wire as the counter electrode. The electrolyte consisted of 5 mM $FeCl_2$ by dissolving $FeCl_2 \cdot 6H_2O$ salt (Aldrich, 99%) in an aqueous solution with 200 mM boric acid as the supporting electrolyte. The pH of the electrolyte solution was then adjusted to 6.5 with 250 mM NaOH (Aldrich, 99.9%). After deoxygenation with N_2 for 30 min, the electrolyte was mixed with GOx from *Aspergillus niger* (Fulka) to obtain 75 μM GOx in the solution. In this freshly prepared electrolyte solution, electrodeposition was conducted at 4 °C by amperometry potentiostatically at −1.2 V vs Ag/AgCl for an appropriate deposition time. The resulting electrodeposits were washed thoroughly with filtered deionized water (18.2 MΩ·cm) and stored in N_2 at room temperature for further analysis. Fe-p53p HNPs were prepared using the same method described above for Fe-GOx HNPs. The p53p peptide, with the sequence of SQETFSDLWKLLPEN,[26] was chemically synthesized using standard Fmoc solid-phase chemistry[27] at St Jude Children's Research Hospital Peptide Facility. The synthetic peptides were purified by HPLC using a reverse-phase C18 semipreparative column with an acetonitrile gradient of 10−35%. The purity of the peptides was verified by a reversed-phase analytical HPLC column and the identity of the final products was verified by mass spectral analysis. The isoelectric point of p53p is 4.0, which is similar to that of GOx (4.2). The same concentration of p53p (as that of GOx, i.e., 75 μM) was added to a solution of 5 mM $FeCl_2$ with a pH of 6.5. The electrodeposition was also carried out at 4 °C followed by a thorough wash with filtered deionized water and kept at 4 °C for bioactivity tests.

Analysis of the HNPs. The surface morphology of the so-prepared samples of Fe-GOx and Fe-p53p HNPs were characterized by field-emission scanning electron microscopy (SEM) (Zeiss LEO FE-SEM 1530 microscope) and by helium ion microscopy (HIM) (Zeiss Orion Plus microscope). Multicross-sectional imaging was conducted using a Zeiss Auriga focused ion beam (FIB) SEM system. The samples were first coated by a thin carbon layer to protect the top surface from damage due to the sputtering Ga ion beam. Very thin slices of the samples with thickness no larger than 1 μm (containing selected NPs on top of the Si substrate) were cut vertically along the surface normal (i.e., in the depth direction of the substrate). SEM images of the exposed cross sections were then collected by using the backscattered electron detector in order to differentiate elements with different atomic masses based on the image contrast. Subsequent cross-sectional SEM images were collected interleavingly after removing additional vertical slices (10 nm thick) from the samples. Crystal structures of HNPs were also determined by glancing-incidence X-ray diffraction (XRD) (PANalytical X'Pert Pro MRD diffractometer) with Cu Kα (1.542 Å) radiation at an incidence angle of 0.5°.

Chemical-state composition of the HNPs was analyzed as a function of Ar ion sputtering time by depth-profiling X-ray photoelectron spectroscopy (XPS) (Thermo-VG Scientific ESCALab 250 microprobe), equipped with a monochromatic Al Kα radiation (1486.6 eV) and operated with a typical energy resolution of 0.4−0.5 full width at half-maximum (fwhm). Three-dimensional (3D) chemical mapping of the HNPs was conducted by time-of-flight (TOF) secondary ion mass spectrometry (SIMS) (ION-TOF SIMS-5 system), equipped with a 2 m long TOF reflectron analyzer and a multichannel detector along with a Bi_3^+ liquid metal analysis ion source and an O_2^+ sputtering ion source. More details on the chemical mapping procedure can be found in the Supporting Information. For the kinetics studies, absorption spectra were collected using a Perkin-Elmer Lambda 35 UV−vis spectrometer equipped with a Labsphere integrating sphere. Magnetic properties were studied in a Quantum Design Dynacool vibrating sample magnetometer (VSM).

Cellular Assay. To test the biocompatibility of the HNPs, cells were cultured on substrates with attached HNPs. Before the cellular assays, the HNPs were sterilized with 70% ethanol. HeLa cells (HeLa, no: CCL-2; ATCC)) were cultured in Dulbecco's modified Eagle's medium with 10% fetal bovine serum and 1% penicillin-streptomycin (ATCC). Cells were maintained in 5% CO_2 in humidity at 37 °C. For live cell imaging experiments, $1-2 \times 10^4$ cells were seeded on glass cover slips and allowed to attach overnight. The cells were then cultured and observed for several days.

Selective Binding of Mdm2-GST to Fe-p53p. A Mdm2-GST solution with concentration of 61 μM was prepared to check the binding of p53p-Mdm2 after hybridization. Details about the preparation of Mdm2 and Mdm2-GST are given in the Supporting Information. The binding of p53p with Mdm2 is sufficiently strong that no separation was found even upon vigorous washing during synthesis. The presence of Mdm2 could therefore be revealed in the corresponding SEM images.

■ RESULTS AND DISCUSSION

Fe-GOx HNPs was prepared at 4 °C by co-electrodeposition of Fe and GOx on a H-terminated Si(100) substrate in a three-electrode cell. The electrolyte solution consisted of 5 mM $FeCl_2$ mixed with an appropriate amount of GOx from asparagines to obtain a concentration of 75 μM GOx in a 200 mM boric acid solution. In order to take advantage of the electrostatic attraction between GOx (with an isoelectric point of 4.2) and Fe^{2+} ions, the solution was maintained at pH 6.5 such that GOx became partially negative. UV−vis spectroscopy was used to monitor the change in the absorption band of GOx (Figure S1a, Supporting Information). The Fe electrolyte (i.e., Fe^{2+}) exhibits a featureless spectrum with no discernible peaks in the region of interest, while the GOx spectrum shows a strong, sharp absorption peak at 274 nm along with weaker, broader bands at 377 and 454 nm, all of which correspond to the oxidized form of flavin groups.[28,29] The Fe-GOx electrolyte, however, exhibits a peak at 273 nm with a shift in the broad bands to 383 and 452 nm, respectively.

Formation of GOx-Fe complex is possible because of the many functional groups, such as amine, imidazole, and sulfhydryl groups, in GOx that could interact with oxidizing mediators. Although both cationic and anionic groups are located on the GOx surface, the enzyme molecule has an essentially negative electrostatic surface potential at pH 6.5 as a result of excess glutamate and aspartate over lysine and arginine.[30,31] The presence of this negative surface potential favors electrostatic complexation of the anionic sites of the enzyme with mediators containing positively charged groups. In an aqueous environment, $FeCl_2$ tends to form $FeOH^+$ monomers,[32−34] with a significantly higher ionic mobility than the considerably larger GOx molecule. The resulting $FeOH^+$ could therefore attach to the anionic sites of GOx through a charge-transfer bond.

To further investigate the Fe-GOx complexation, we performed cyclic voltammetry on the Fe-GOx electrolyte (Figure S1b, Supporting Information) and compared the result with those on the pristine GOx electrolyte and Fe electrolyte in UV experiments (Figure S1a, Supporting Information). In the absence of GOx, oxidation of Fe^{2+} to Fe^{3+} complex species occurs at an anodic peak potential of 2 mV (vs Ag/AgCl), while reduction occurs at a cathodic potential of −450 mV (vs Ag/AgCl) upon the reverse scan. In the presence of GOx, both anodic and cathodic peak potentials are shifted to more positive values, with the shift in the cathodic peak potential (from −450 mV to −370 mV) found to be discernibly larger than that of the anodic peak potential (from 2 mV to 5 mV). The smaller reduction potential needed for Fe^{3+} to Fe^{2+} in the presence of GOx confirms the complex formation of the Fe species that changes the reduction potential, in good accord with our UV−vis spectroscopic results. A decrease in the corresponding current density is also observed, which can be attributed to the slower diffusion of $FeOH^+$ when bound to a large and slowly moving GOx molecule. In general, the concentrations of the redox species and the number of electrons involved in the reactions control their diffusion coefficients and the resulting current densities.[35] As these voltammograms were obtained under the same experimental conditions, the observed difference in the current density is attributed to the difference in diffusion coefficients. The diffusion coefficient for $FeOH^+$ is expected to be smaller upon binding with GOx. A similar observation has been reported for the $[Fe^{II}(phen)_3]^{2+}$ when bounded to GOx and to DNA.[36,37]

Using the Fe-GOx complexes as our precursors, we synthesized the HNPs. In a freshly prepared Fe-GOx electrolyte solution, homogeneous spherical NPs were deposited on the H-terminated Si substrate by amperometry at −1.2 V (vs Ag/AgCl). These NPs exhibit a remarkably narrow size distribution, with the average size easily controllable from 30 nm to 3.5 μm by varying the respective deposition time from 10 s to 60 min (Figure S2, Supporting Information). Figure 1a shows a typical HIM image of Fe-GOx HNPs obtained by a 30 min deposition. Furthermore, these nanograins are made up of nanocrystallites of 18 nm diameter in size (Figure 1b), as estimated by applying the Scherrer analysis to the Fe(110) diffraction peak in the corresponding X-ray diffraction pattern (Figure 1d). The features in the XRD pattern (Figure 1d) correspond to the bcc phase of metallic Fe (PDF2 006−0696).

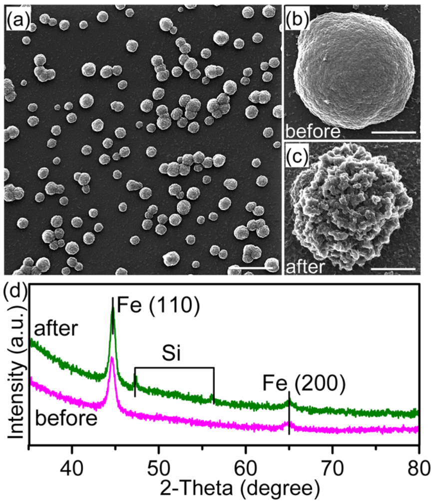

Figure 1. HIM images of Fe-GOx HNPs (a) and (b) before and (c) after the activity test, and (d) their corresponding glancing incidence XRD patterns before (bottom curve) and after the activity test (top curve). Scale bars represent 5 μm in (a) and 1 μm in (b) and (c).

To confirm the activity of GOx after electrodeposition, we used a glucose spectrometric assay to monitor the production of H_2O_2 by detecting quinoneimine dye (with details given in Figure S3, Supporting Information). The characteristic absorption band of the dye at 510 nm is found to become more intense over 15 min, which indicates that GOx remains bioactive upon hybridization into the NPs. After the bioactivity test, the sample was washed thoroughly with filtered deionized water, which also makes the porous structure of the HNPs more obvious (Figure 1c). The appearance of the porous

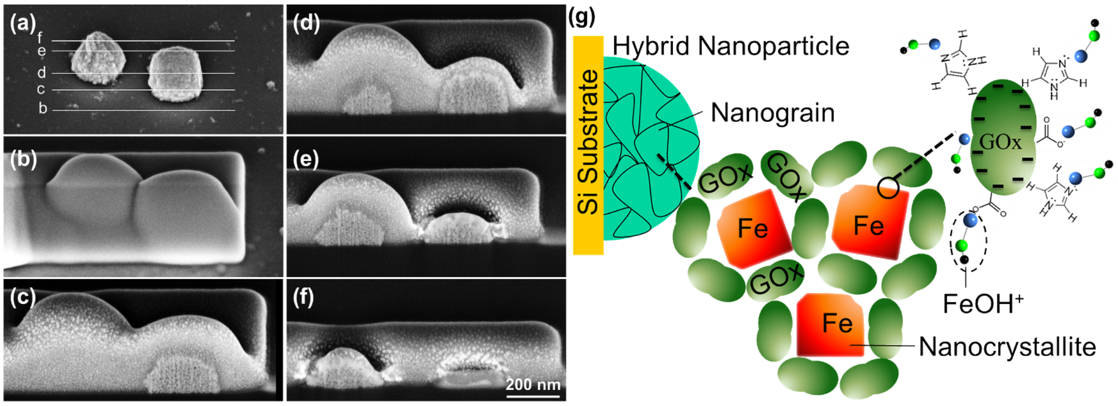

Figure 2. Backscattered electron SEM images of (a) the top view of two Fe-GOx HNPs before cross-sectional imaging and (b−f) cross-sectional views of selected vertical cuts at the locations marked in (a). (g) Schematic "stone-and-mortar" model for Fe-GOx HNPs electrodeposited on a Si substrate.

structure suggests diffusion of glucose into the Fe-GOx HNPs to reach the active sites of GOx, which causes the nanograins to cluster into larger grains resulting in a more porous appearance for the NPs. The average nanocrystallite size also increases from 18 to 24 nm as estimated from their respective XRD patterns (Figure 1d). This suggests the presence of GOx in the deeper layers of NPs and not just on the surface. It should be noted that the XRD features obtained after the activity test also correspond to the bcc phase of metallic Fe. We also soaked the Fe-GOx HNPs in H_2O_2 overnight. No increase in porosity or grain clustering was observed, which confirms that such an increase in porosity is caused by glucose reaction with HNPs, thereby validating the unique activity of the HNP. No increase in porosity was observed upon the glucose activity test on the pristine Fe NP sample (i.e., without GOx).

The presence of nanosized grains throughout a HNP can also be observed in the tomography images obtained by using the multicross-sectional imaging technique in a FIB-SEM.[38,39] This technique allows us to observe nanostructures buried within the bulk with a spatial resolution of 10 nm. The SEM image obtained with the backscattered detector in Figure 2a shows the top view of two Fe-GOx HNPs, with the lines marking the vertical cut locations for the selected cross-sectional images, shown in Figure 2b−f. The black spots inside the NPs correspond to voids and/or elements with lower masses, likely reflecting the locations of GOx, among the brighter Fe nanocrystallites. From the series of cross-sectional images, it is evident that the observed HNPs consist of very small Fe subunits of nanocrystallites separated by voids and/or organic materials. The fairly uniform distribution of these GOx locations observed inside the nanoparticles leads us to propose a "stone-and-mortar" model for the HNP, shown schematically in Figure 2g. In this model, individual nanograins (in a Fe-GOx HNP) consist of Fe nanocrystallites "sticking" together by GOx molecules. Inside a nanograin, GOx could serve as the substrate, providing nucleation sites for Fe crystallization, which could proceed by reduction of FeOH$^+$ ions adsorbed on the GOx substrate through its interaction with the partially negative amino acid components (e.g., glutamate and asparatate) of the GOx. FeOH$^+$ ions undergo adsorption onto the GOx followed by reduction to metallic Fe, i.e., $FeOH^+(ads) + H^+ + 2e^- \rightarrow Fe + H_2O$. However, to distinguish between an actual void and an organic intermediate layer would require additional analysis by a complementary method, such as 3D chemical imaging provided by the SIMS technique.

One possible configuration for the hybridization of Fe and GOx is that the NPs consist of nanocrystallites individually covered by GOx. In this configuration, it should be possible to observe the GOx inside the NP even when all the GOx molecules on the surface of the NP are removed. To confirm the presence of GOx along with Fe inside the HNPs, we conduct 3D chemical imaging by TOF-SIMS. This method enables us to probe the composition of the bulk materials at different depth, which makes possible studies not just of 3D composition of biomaterials but also of diffusion of a component into a semiconductor material.[40,41] We have chosen relatively large HNPs (2.5 μm) for this experiment in order to increase the accuracy of the characterization, but the results are expected to be similar for all sizes. A 300 × 300 μm^2 area of the sample was precleaned with O^{2+} sputtering for 5 s before imaging. The secondary ions were mass-separated in a 2 m long TOF reflectron analyzer, and the appropriate secondary ions Fe$^+$, NaNH^{2+} for GOx, and Si$^+$ were collected over a rastered sampling area of 100 × 100 μm^2 to obtain a 2D map. The sample was then sputtered with O_2^+ to remove the sample layer-by-layer at a well-defined sputtering rate. The 2D maps were collected interleavingly between the sputtered layers as a function of sputtering depth to obtain the depth profiles and to construct the corresponding 3D images of the Fe, GOx, and Si components. Figure 3a shows the 3D images obtained for three component ions and their overlap (total) for a typical sample of HNPs. The presence of the enzyme component only on the Fe component (i.e., nanoparticle) and not on the bare surface of the Si substrate can clearly be seen in the corresponding topmost 2D maps shown in Figure S4, Supporting Information. We also show as insets in Figure 3a a magnified view of a selected area of the topmost 2D maps marked by a small square in Figure 3a, top rightmost panel. Figure 3b shows the *YZ* cross sections of the respective 3D images in Figure 3a for a selected *X* position. Evidently, the concurrence of component intensities at the same location shown in Figure 3b further confirms the presence of both Fe and GOx throughout the NPs, indicating their hybrid nature. The *YZ* cross-sectional maps are plotted with an extended *Z* scale to better illustrate the details in the depth direction. The similar decreasing trends found for the Fe and GOx components with depth are also clearly observed in the corresponding depth profiles shown in Figure S5.

The depth-profiling XPS data shown in Figure 4 provides collaborative support for our SIMS observation. For the as-prepared sample, the C 1s peaks at 284.8, 286.2, and 288.4 eV

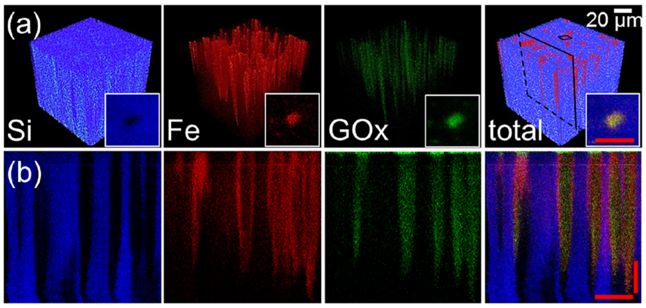

Figure 3. (a) TOF-SIMS 3D images of Si^+ (blue), Fe^+ (red), and $NaNH^{2+}$ (corresponding to GOx; green), and their overlap (total) for Fe-GOx HNPs on a 100 × 100 μm^2 area of the sample, with the insets depicting their corresponding topmost 2D maps of a selected Fe-GOx HNP in this sampling area (marked by small square in top rightmost panel). The scale bar for the insets is 2 μm. (b) Selected *YZ* cross sections of the corresponding 3D images of Fe-GOx HNPs (at an *X* location as marked in the image cube in (a), top rightmost panel). The horizontal (*Y*) and vertical (*Z*) scale bars correspond to 2 μm and 200 nm, respectively.

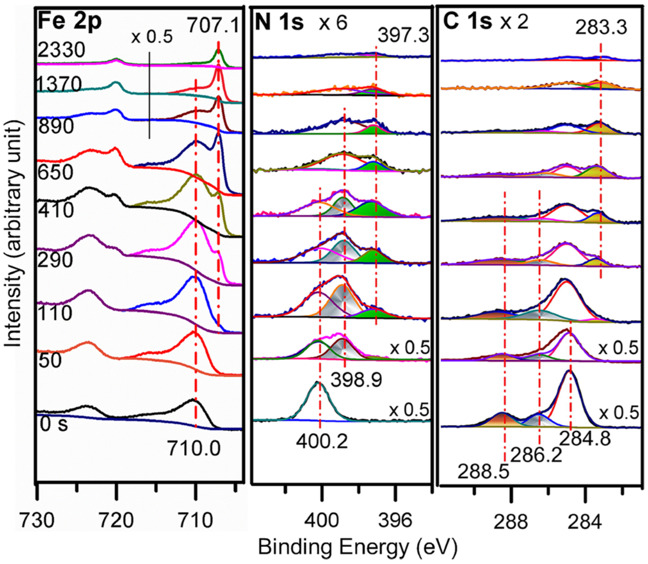

Figure 4. Depth-profiling XPS spectra of Fe 2p, N 1s, and C 1s regions for the as-prepared Fe-GOx HNPs and upon Ar sputtering for 50, 110, 290, 410, 650, 890, 1370, and 2330 s.

can be attributed, respectively, to the C−H, C−O, and C═O components of the amino acid side chains of the polypeptide backbone of GOx.[42,43] Similarly, the N 1s features at 398.9 and 400.2 eV correspond to the NH_2 and NHC═O components,[44,45] respectively. Upon sputtering for 110 s, dramatic reductions in the intensities of these C 1s and N 1s components are observed. Additional C 1s feature found at 283.3 eV and N 1s feature at 397.3 eV can be assigned to C−Fe[46] and N−Fe features,[47] respectively, indicating the interaction between GOx and Fe nanocrystallites. After 290 s of sputtering, the Fe $2p_{3/2}$ peak at 710.0 eV and the shoulder emerged at 707.1 eV can be attributed to Fe oxides and metallic Fe, respectively.[47] From our sputtering rate, we estimate that this initial sputtering corresponds to the removal of a 4−5 nm thick layer of material, consistent with one monolayer of physisorbed GOx (uniformly distributed on both the HNPs and Si substrate). Continued sputtering for over 650 s reveals that the relative-intensity reductions of the C−Fe and N−Fe features parallel those of the other C and N components of GOx and of the metallic Fe. The similar trends found in the intensity reductions, along with the presence of N and C even after extended Ar sputtering (into the deeper layers), provide strong support for the intermixing of GOx with Fe nanocrystallites inside the HNP.

To further investigate the nature of the Fe−C and Fe−N bonds found between GOx and Fe before formation of the HNP and the role of these bonds in the evolution of the HNP, we prepared drop-cast thin films of electrolytes containing GOx with $FeCl_2$ (Fe-GOx electrolyte) and without $FeCl_2$ (GOx electrolyte) before amperometry. Their C 1s and N 1s spectra are compared with those of HNPs (after 290 s of sputtering) in Figure 5. (It should be noted that a brief sputtering was used to remove any surface carbonaceous layer often found due to sample handling in air.) Evidently, the drop-cast film of the Fe-GOx electrolyte exhibits all the C 1s and N 1s features as those of the GOx electrolyte, but with additional C 1s feature at 283.3 eV and N 1s feature at 397.3 eV. The similar relative intensities of the common C 1s and N 1s features for the GOx electrolyte to those found for Fe-GOx electrolyte indicate that the GOx molecules interact with Fe without dissociation. The observed additional features for the Fe-GOx electrolyte are found at the same binding energy locations as the respective features in the Fe-GOx HNPs, which indicates that the HNPs contain Fe-GOx complexes as their building blocks (before nanocrystallite formation). The differences in the relative intensities of the C 1s and N 1s features for Fe-GOx HNPs from those for the drop-cast film of Fe-GOx electrolyte suggest that there are more GOx interactions with Fe involving the NHC═O group and C−O group in the HNPs than the drop-cast film.

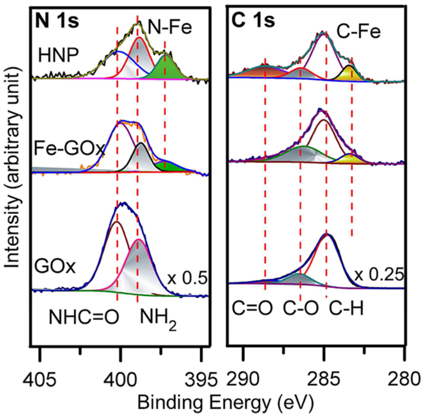

Figure 5. XPS spectra of N 1s and C 1s regions for drop-cast films of pristine GOx and of Fe-GOx electrolytes and for Fe-GOx HNPs, all after 290 s sputtering.

In order to investigate the biocompatibility of the Fe-GOx HNPs, we studied the effect of HNPs on cell proliferation. To be safe for use in the human body, Fe oxides usually need to be coated with a biocompatible shell. These shells are mainly polymeric materials that should be water-soluble and non-cytotoxic. However, in addition to adding an extra step to the synthesis, the main drawback of polymeric coating is their poor long-term chemical stability of the inorganic core.[48−51] We therefore have not used any coating in the present experiment. In particular, we used the Fe-GOx NPs directly deposited on an ITO-glass substrate and evaluated their effects on HeLa cells. In the present experiment, we employed ITO-glass instead of H−

Si as the conductive substrate in order to obtain optical images of the samples. It should be noted that the respective SEM images show no difference in the morphologies of HNPs deposited on ITO-glass and H−Si substrates. HeLa cells were seeded on ITO-glass substrates with the predeposited Fe-GOx HNPs, and cell growth was then monitored by bright-field optical microscopy for 5 days (Figure 6a). Some parts of the samples were scratched to remove the HNP cell seeding, and these were used as the control so as to allow comparison with the areas with HNPs. As shown in Figure 6b, cell seeding density, morphology, and growth appear to be similar in the bright regions (without HNPs) and in the darker areas (with HNPs). In other words, the cells are able to grow on the substrates coated with the Fe-GOx HNPs as on substrates without the Fe-GOx HNPs.

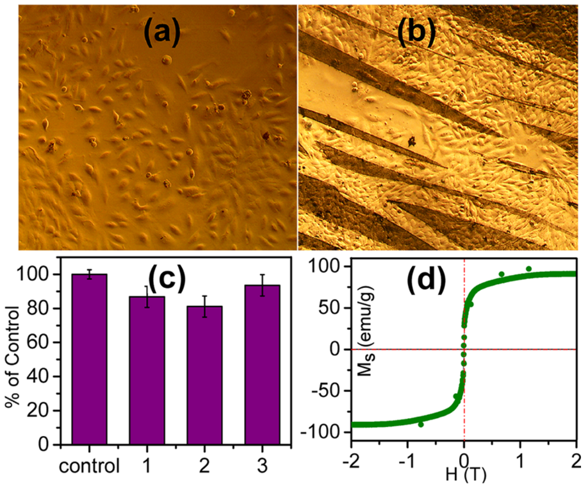

Figure 6. Optical images of HeLa cells grown on ITO-glass substrate coated with Fe-GOx HNPs, 400 nm in average size, after 5 days: (a) without and (b) with sample scratching. (c) MTT data quantifying consistently high viability of human hepatoma cells after 5 days of culturing on three separate ITO-glass substrates coated with Fe-GOx HNPs relative to control (cultured on a plain ITO-glass substrate). (d) Magnetization curve of the Fe-GOx HNPs (with an average size of 400 nm).

Furthermore, in order to metabolically quantify the amount of active cells after exposure to Fe-GOx HNPs, we performed MTT (3-[4,5-dimethyl-2-thiazol]-2,5-diphenyl-2H-tetrazolium bromide) reduction experiments involving more delicate cells. Human hepatoma cells (liver, PLC/PRF/5, ATCC no: CRL-8024) were cultured in eagle's minimum essential medium (EMEM) American Type Culture Collection (ATCC) with 10% fetal bovine serum and 1% penicillin-streptomycin. The cells were maintained in 5% CO_2 in humidity at 37 °C. Before incubating the cells on the substrates, each substrate has been sterilized by first immersing in 70% ethanol thrice (10 min each), followed by PBS rinse. The substrates were subsequently irradiated with UV light for 2 h before use. Liver cells (10,000 cells) were then seeded onto each substrate in a 12-well plate and incubated for 24 h at 37 °C. We employed the procedure for the MTT assay as outlined by the supplier (Sigma-Aldrich). Figure 6c depicts the results from the MTT assay, which has been performed in triplicates. Our results show quantitatively the cell population and activity on the three substrates coated with Fe-GOx HNPs compared to that on a plain ITO-glass used as the control. Only a slight difference is observed, indicating that these Fe-GOx HNPs are cell-safe and have no obvious detrimental effect on viability and cell growth.

Figure 6d shows the magnetization curve of the Fe-GOx HNPs (with an average size of 400 nm) as determined by using a VSM. Evidently, the lack of hysteresis, along with the observed 90 emu/g saturation magnetization, indicates that the Fe-GOx HNPs exhibit superparamagetic behavior. Due to the metallic nature of Fe in Fe-GOx HNPs, the saturation magnetization has a much larger value than the reported values for superparamagnetic iron oxide NPs in the literature.[52,53] The high saturation magnetization is especially important for NPs when they are used as a contrast agent for MRI application. It should be noted that the size of the superparamagnetic NPs cannot exceed 10 nm for Fe oxide and 20 nm for Fe.[54−56] However, for in vivo applications, magnetic NPs should have an appropriate size of 10−100 nm to maintain longer circulation times, because NPs smaller than 10 nm are removed by renal clearance.[57] For this reason, they are usually coated with a (polymer or organic) shell to obtain the desired size.[52] The present superparamagnetic Fe-GOx HNPs are therefore quite remarkable because the size of superparamagnetic HNPs can be

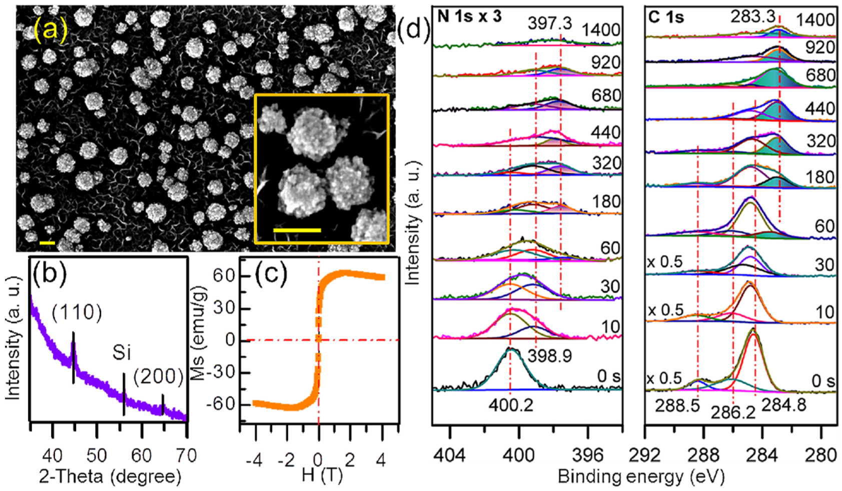

Figure 7. (a) SEM images (scale bars are 200 nm), (b) XRD pattern, (c) hysteresis loop, (d) depth-profiling XPS spectra of N 1s and C 1s regions of Fe-p53p HNPs obtained after 600 s deposition.

easily controlled during the co-electrodeposition, thereby allowing us to eliminate the extra coating step. Since the present HNPs are much larger than the superparamagnetic NP size regime, the observed behavior supports our structural model shown schematically in Figure 2g. In other words, if the nanograins were just surface-functionalized by the GOx (i.e., without any hybridization), then the nanocrystallites inside a nanograin are not isolated from one another by the GOx. In this case, the NP should exhibit ferromagnetic and not the observed superparamagnetic behavior.

To demonstrate the general applicability of the present approach to other biomolecules even with different sizes and the application of HNPs to targeted drug delivery, we prepared Fe-p53p HNPs at 4 °C by co-electrodeposition of Fe and p53p on a H-terminated Si(100) substrate in a three-electrode cell. (It should be noted that p53p is approximately 100 times smaller than GOx.) The electrolyte solution consisted of 5 mM $FeCl_2$ and 75 μM p53p and 200 mM boric acid. The pH was adjusted to 6.5 before adding p53p to the solution. Deposition was carried out at −1.2 V vs Ag/AgCl for different amounts of deposition time. Figure 7a shows the SEM image of typical Fe-p53p HNPs after 600 s deposition. The corresponding XRD pattern (Figure 7b) shows metallic Fe with an average grain size of 22 nm, which accounts for the observed rough surfaces of HNPs in the SEM image. Similar to Fe-GOx HNPs, these Fe-p53p HNPs also exhibit superparamagnetic behavior with 60 emu/g saturation magnetization and no hysteresis (Figure 7c). The depth-profiling XPS spectra for the N 1s and C 1s regions in Figure 7d indicate the presence of N−Fe and C−Fe features at 397.3 and 283.3 eV, respectively. The emergence of these features only upon longer sputtering time (1400 s) confirms the intermixing of Fe with p53p in the core (i.e., subsurface) region and the hybrid nature of NPs. To verify that the p53p in the HNP does not change after hybridization and preserves its bioactivity, we examine p53p-Mdm2 bonding ability. For this purpose, we incubated pristine Fe NPs and Fe-p53p HNPs in the solution of Mdm2-GST for 4 h. We then washed both samples thoroughly with deionized water. The SEM images obtained after incubation show extra materials on top of Fe-p53p HNPs but not on pristine Fe NPs, which confirms the attachment of Mdm2 to p53p and therefore the bioactivity of p53p in the HNP (Figure S6, Supporting Information).

CONCLUSIONS

In summary, Fe-GOx and Fe-p53p HNPs have been successfully obtained by electrodeposition of Fe-GOx and Fe-p53p complexes directly as the building blocks of the nanograins at 4 °C. We propose a “stone-and-mortar” architecture for the HNP, in which GOx or p53p molecules behave as the mortar to keep the Fe nanocrystallites together. HIM and FIB-SEM multi cross-sectional studies both show the nanograins interconnected to one another by the GOx or p53p molecules in the HNPs. Furthermore, both TOF-SIMS and depth-profiling XPS results further confirm the intermixed nature of the Fe-biomolecule NPs, in which the biomolecules are incorporated throughout the HNP without affecting their bioactivity. Of special interest is that hybridization of Fe-GOx and Fe-p53p HNPs is obtained by complex formation of Fe with the biomolecule (GOx or p53p) before deposition onto the substrate and the growth is maintained by these Fe-biomolecule complexes as the building blocks. Furthermore, these HNPs are found to be superparamagnetic and could be made in the desirable size regime. As demonstrated by their apparent lack of any detrimental effect on cell growth, their biocompatibility, together with their strong magnetic properties, make these HNPs promising agents for MRI and targeted drug delivery systems. These HNPs can be easily harvested from the substrate and dispersed in an aqueous solution by sonication. Incorporating two different biomolecules with very different sizes confirms the general applicability of the present synthetic approach. The present method of incorporating bioactive molecules into magnetic (and nonmagnetic) nanostructures is therefore not limited to GOx or p53p. Hybridization of GOx as a water-soluble enzyme and p53p as an anticancer peptide with magnetic nanostructures therefore offers an effective immobilization method to enable them for use not only as reusable sensors and magnetic contrast agents but also in greatly improved drug delivery and recovery systems.

ASSOCIATED CONTENT

Supporting Information

Experimental details, UV and CV data, SEM images, TOF-SIMS mapping and depth profile. This material is available free of charge via the Internet at http://pubs.acs.org.

AUTHOR INFORMATION

Corresponding Author

tong@uwaterloo.ca

Notes

The authors declare no competing financial interest.

ACKNOWLEDGMENTS

This work was supported by the Natural Sciences and Engineering Research Council of Canada.

REFERENCES

(1) Katz, E.; Willner, I. *Angew. Chem., Int. Ed. Engl.* **2004**, *43*, 6042−6108.

(2) Niemeyer, C. M. *Angew. Chem., Int. Ed. Engl.* **2001**, *40*, 4128−4158.

(3) Katz, E.; Sheeney-Haj-Ichia, L.; Willner, I. *Chemistry* **2002**, *8*, 4138−4148.

(4) Mornet, S.; Vekris, A.; Bonnet, J.; Duguet, E.; Grasset, F.; Choy, J. H.; Portier, J. *Mater. Lett.* **2000**, *42*, 183−188.

(5) Indira, T. K.; Lakshmi, P. K. *Int. J. Pharm. Sci. Nanotechnol.* **2010**, *3*, 1035−1042.

(6) Yu, C.-C.; Kuo, Y.-Y.; Liang, C.-F.; Chien, W.-T.; Wu, H.-T.; Chang, T.-C.; Jan, F.-D.; Lin, C.-C. *Bioconjugate Chem.* **2012**, *23*, 714−724.

(7) Ansari, S. A.; Husain, Q. *Biotechnol. Adv.* **2012**, *30*, 512−523.

(8) Saraswati, T. E.; Ogino, A.; Nagatsu, M. *Carbon* **2012**, *50*, 1253−1261.

(9) Xing, Z.-C.; Chang, Y.; Kang, I.-K. *Sci. Technol. Adv. Mater.* **2010**, *11*, 014101.

(10) Kandimalla, V.; Tripathi, V.; Ju, H. *Crit. Rev. Anal. Chem.* **2006**, *36*, 73−106.

(11) Rendl, M.; Bönisch, A.; Mader, A.; Schuh, K.; Prucker, O.; Brandstetter, T.; Rühe, J. *Langmuir* **2011**, *27*, 6116−6123.

(12) Ricci, F.; Palleschi, G. *Biosens. Bioelectron.* **2005**, *21*, 389−407.

(13) Luo, X.-L.; Xu, J.-J.; Du, Y.; Chen, H.-Y. *Anal. Biochem.* **2004**, *334*, 284−289.

(14) Shi, L.; Xiao, Y.; Willner, I. *Electrochem. commun.* **2004**, *6*, 1057−1060.

(15) Wang, J. *Chem. Rev.* **2008**, *108*, 814−825.

(16) Toghill, K. E.; Compton, R. G. *Int. J. Electrochem. Sci.* **2010**, *5*, 1246−1301.

(17) Ivnitski, D.; Branch, B.; Atanassov, P.; Apblett, C. *Electrochem. Commun.* **2006**, *8*, 1204−1210.

(18) Holzapfel, W. H.; Geisen, R.; Schillinger, U. *Int. J. Food Microbiol.* **1995**, *24*, 343−362.

(19) Ma, Z.; Ding, T. *Nanoscale Res. Lett.* **2009**, *4*, 1236−1240.

(20) Wei, A.; Sun, X. W.; Wang, J. X.; Lei, Y.; Cai, X. P.; Li, C. M.; Dong, Z. L.; Huang, W. *Appl. Phys. Lett.* **2006**, *89*, 123902.

(21) Bharathi, S.; Nogami, M. *Analyst* **2001**, *126*, 1919−1922.

(22) Crumbliss, A. L.; Perine, S. C.; Stonehuerner, J.; Tubergen, K. R.; Zhao, J.; Henkens, R. W.; O'Daly, J. P. *Biotechnol. Bioeng.* **1992**, *40*, 483−490.

(23) Baek, S.; Kutchukian, P. S.; Verdine, G. L.; Huber, R.; Holak, T. A.; Lee, K. W.; Popowicz, G. M. *J. Am. Chem. Soc.* **2012**, *134*, 103−106.

(24) Wade, M.; Li, Y.-C.; Wahl, G. M. *Nat. Rev. Cancer* **2013**, *13*, 83−96.

(25) Saha, M. N.; Qiu, L.; Chang, H. *J. Hematol. Oncol.* **2013**, *6*, 23.

(26) Pazgier, M.; Liu, M.; Zou, G.; Yuan, W.; Li, C.; Li, C.; Li, J.; Monbo, J.; Zella, D.; Tarasov, S. G.; Lu, W. *Proc. Natl. Acad. Sci. U. S. A.* **2009**, *106*, 4665−4670.

(27) Merrifield, R. B. *J. Am. Chem. Soc.* **1963**, *85*, 2149−2154.

(28) Stoscheck, C. M. *Methods Enzymol.* **1990**, *182*, 50−68.

(29) Zhou, K.; Zhu, Y.; Yang, X.; Li, C. *Electroanalysis* **2010**, *22*, 259−264.

(30) Lvov, Y.; Katsuhiko, A.; Ichinose, I.; Kunitake, T. *J. Am. Chem. Soc.* **1995**, *117*, 6117−6123.

(31) Hodak, J.; Etchenique, R.; Calvo, E. J.; Singhal, K.; Bartlett, P. N. *Langmuir* **1997**, *13*, 2708−2716.

(32) Mohapatra, M.; Mohapatra, L.; Anand, S.; Mishra, B. K. *J. Chem. Eng. data* **2010**, *55*, 1486−1491.

(33) Liu, L.; Kou, H.-Z.; Mo, W.; Liu, H.; Wang, Y. *J. Phys. Chem. B* **2006**, *110*, 15218−15223.

(34) Boily, J.-F.; Lutzenkirchen, J.; Balmes, O.; Beattie, J.; Sjoberg, S. *Colloids Surf.* **2006**, *179*, 11−27.

(35) Hamann, C. H. *Electrochemistry*; 2nd ed.; WILEY-VCH Verlag GmbH & Co. KGaA: New York, 2007.

(36) Morikawa, M.; Kimizula, N.; Yoshihara, M.; Endo, T. *Chem.—Eur. J.* **2002**, *8*, 5580−5584.

(37) Carter, M. T.; Rodriguez, M.; Bard, A. J. *J. Am. Chem. Soc.* **1989**, *111*, 8901−8911.

(38) Inkson, B.; Mulvihill, M.; Möbus, G. *Scr. Mater.* **2001**, *45*, 753−758.

(39) Schaffer, M.; Wagner, J.; Schaffer, B.; Schmied, M.; Mulders, H. *Ultramicroscopy* **2007**, *107*, 587−597.

(40) Passarelli, M. K.; Winograd, N. *Biochim. Biophys. Acta* **2011**, *1811*, 976−990.

(41) Hill, R.; Blenkinsopp, P.; Thompson, S.; Vickerman, J.; Fletcher, J. S. *Surf. Interface Anal.* **2011**, *43*, 506−509.

(42) De Benedetto, G. E.; Malitesta, C.; Zambonin, C. G. *J. Chem. Soc. Faraday Trans.* **1994**, *90*, 1495−1499.

(43) Guiomar, A. J.; Guthrie, J. T.; Evans, S. D. *Langmuir* **1999**, *15*, 1198−1207.

(44) Jagst, E. Surface Functional Group Characterization Using Chemical Derivatization X-Ray Photoelectron Spectroscopy (CD-XPS). *Ph.D.*, University of Berlin, Berlin, 2011

(45) Liu, X. *Biosens. Bioelectron.* **2004**, *19*, 823−834.

(46) Bonnet, F.; Ropital, F.; Lecour, P.; Espinat, D.; Huiban, Y.; Gengembre, L.; Berthier, Y.; Marcus, P. *Surf. Interface Anal.* **2002**, *34*, 418−422.

(47) Mooulder, J. F.; Stickle, W. F.; Sobol, P. E.; B, K. D. *Handbook of X-Ray Photoelectron Spectroscopy*, 2nd ed.; Chastain, J., Ed.; Perkin-Elmer Corp.: Eden Prairie, MN, 1992.

(48) Mahmoudi, M.; Laurent, S.; Shokrgozar, M. A.; Hosseinkhani, M. *ACS Nano* **2011**, *5*, 7263−7276.

(49) Mahmoudi, M.; Hofmann, H.; Rothen-Rutishauser, B.; Petri-Fink, A. *Chem. Rev.* **2012**, *112*, 2323−2338.

(50) Shi, S.-F.; Jia, J.-F.; Guo, X.-K.; Zhao, Y.-P.; Chen, D.-S.; Guo, Y.-Y.; Cheng, T.; Zhang, X.-L. *Int. J. Nanomed.* **2012**, *7*, 5593−5602.

(51) Babiuch, K.; Wyrwa, R.; Wagner, K.; Seemann, T.; Hoeppener, S.; Becer, C. R.; Linke, R.; Gottschaldt, M.; Weisser, J.; Schnabelrauch, M.; Schubert, U. S. *Biomacromolecules* **2011**, *12*, 681−691.

(52) Gupta, A. K.; Gupta, M. *Biomaterials* **2005**, *26*, 3995−4021.

(53) Cheraghipour, E. *J. Biomed. Sci. Eng.* **2012**, *05*, 715−719.

(54) Jeun, M.; Lee, S.; Kyeong Kang, J.; Tomitaka, A.; Wook Kang, K.; Il Kim, Y.; Takemura, Y.; Chung, K.-W.; Kwak, J.; Bae, S. *Appl. Phys. Lett.* **2012**, *100*, 092406.

(55) Tartaj, P.; Serna, C. J. *J. Am. Chem. Soc.* **2003**, *125*, 15754−15755.

(56) Joseyphus, R. J.; Matsumoto, T.; Sato, Y.; Jeyadevan, B.; Tohji, K. *J. Magn. Magn. Mater.* **2007**, *310*, 2393.

(57) Wahajuddin; Arora, S. *Int. J. Nanomed.* **2012**, *7*, 3445−3471.